Ambipolar Transport in Methylammonium Lead Iodide Thin Film Transistors

Jeoungmin Ji, Farjana Haque[ID], Nhu Thi To Hoang[ID] and Mallory Mativenga *[ID]

Department of Information Display, Kyung Hee University, Seoul 130-701, Korea; jjm@khu.ac.kr (J.J.); farjana@tft.khu.ac.kr (F.H.); nhu@tft.khu.ac.kr (N.T.T.H.)
* Correspondence: mallory@khu.ac.kr; Tel.: +82-02-961-9504

Abstract: We report clear room temperature ambipolar transport in ambient-air processed methylammonium lead iodide ($MAPbI_3$) thin-film transistors (TFTs) with aluminum oxide gate-insulators and indium-zinc-oxide source/drain electrodes. The high ionicity of the $MAPbI_3$ leads to p-type and n-type self-doping, and depending on the applied bias we show that simultaneous or selective transport of electrons and/or holes is possible in a single $MAPbI_3$ TFT. The electron transport (n-type), however, is slightly more pronounced than the hole transport (p-type), and the respective channel resistances range from 5–11 and 44–55 MΩ/µm. Both p-type and n-type TFTs show good on-state characteristics for low driving voltages. It is also shown here that the on-state current of the n-type and p-type TFTs is highest in the slightly PbI_2-rich and MAI-rich films, respectively, suggesting controllable n-type or p-type transport by varying precursor ratio.

Keywords: Ambipolar transport; lead iodide; methylammonium; organic-inorganic hybrid; perovskite; thin film transistor

1. Introduction

Hybrid organic-inorganic perovskites are emerging materials with remarkable optoelectronic properties [1]. Among them, methylammonium lead iodide ($CH_3NH_3PbI_3$) has proven to be an exceptional light harvester for solar cells, recording power conversion efficiencies of over 20% in just a few years [2–6]. Despite low-temperature (<150 °C) processing, the density of electronic defect states in $CH_3NH_3PbI_3$ ($MAPbI_3$) is surprisingly low [7–13]. This combined with other unique properties such as high photoluminescence quantum yield, tunable bandgap, and a high absorption coefficient, are the reasons for the success of the $MAPbI_3$ in photovoltaics (PV) [1,14]. In addition to PV applications, $MAPbI_3$ is also appealing for several other applications, including light emitting diodes (LEDs) [8,10,11,15], thin-film transistors (TFTs) [16–21] and light emitting transistors (LETs) [2].

For large-area TFT applications, $MAPbI_3$ enables low manufacturing costs, as it can be synthesized from simple precursors through solution processing or vapor deposition methods [17–22]. Additionally, $MAPbI_3$ possesses high carrier mobility and a bandgap in the near-infrared energies, which can be easily tuned with chemical composition [23–27]. The ability to be fabricated from solution and its potential for high field-effect mobility (μ_{FE}) has been particularly interesting in flexible, printable or wearable devices, where the development of such a semiconductor is key [4].

Due to the existence of both the inorganic and organic components, $MAPbI_3$ has the potential for ambipolar transport, where simultaneous or selective transport of electrons and/or holes is possible. Theoretical calculations have revealed that charged MA, Pb, and I vacancies have low formation energies [28,29], suggesting that the high ionicity of this material may lead to n-type or p-type self-doping. Furthermore, previous studies have shown that carrier concentration can vary over orders of magnitude, depending on the precursor ratio (MAI/PbI_2) and thermal annealing conditions, thus

resulting in preferential n-type or p-type transport characteristics [30]. Ambipolar transport enables the design of circuits with low-power dissipation and good noise margins, similar to those encountered in complementary metal–oxide semiconductor (CMOS) logic circuits. However, nearly all $MAPbI_3$ TFTs in previous studies have been shown to transport only electrons (n-type) [17,18,31,32] with the exception of those measured at and below 198 K with high driving voltages (over 100 V) and/or doped with cesium (Cs) and formamidinium (FA) [2,33].

Here we investigate the room temperature (RT) ambipolar transport in the $MAPbI_3$ TFTs by correlating charge carrier transport with the TFTs' current–voltage (I–V) characteristics. In contrast to previous reports, we process the $MAPbI_3$ in ambient air for room temperature stability and use a thin (32 nm) UV ozone-treated aluminum oxide (AlO_x) gate-insulator (GI) to decrease the driving voltages.

2. Materials and Methods

We fabricated the $MAPbI_3$ TFTs on glass with the inverted coplanar structure (Figure 1). The gate electrode is a 40-nm-thick Mo layer deposited by sputtering at 280 °C. For the gate insulator (G. I), we used a 40-nm-thick AlO_x layer spin coated from solution in ambient air (relative humidity = 50 ± 5, Temperature = 25 °C ± 2 °C). We prepared the AlO_x solution by mixing aluminium chloride ($AlCl_3$) (Merck Korea Ltd./Sigma-Aldrich Korea Ltd.), acetonitrile (35%) (Merck Korea Ltd./Sigma-Aldrich Korea Ltd.), and ethyleneglycol (65%) (0.2 M) (Merck Korea Ltd./Sigma-AldrichKorea Ltd.). The solution is spin coated at 2000 rotations per min (rpm) for 30 s. Two layers were used to achieve the thickness of 40 nm and curing at 250 °C for five minutes was performed to evaporate the solvent, followed by 5 min UV ozone treatment. For film densification, we performed a final anneal for 2 h at 350 °C. Using Mo/AlO_x/indium zinc oxide (IZO) structures (400 μm × 400 μm), the capacitance of the AlOx layer per unit area (C_{OX}) is estimated to be approximately 200 nF/cm^2. We define the source and drain electrodes by patterning a 60 nm thick IZO layer deposited at 280 °C by sputtering. We spin-coated a positive photoresist (PR) (Sigma-Aldrich, Inc., Steinheim, Germany) layer on top of the source and drain electrodes and patterned it to form "banks" into which we spin coated the $MAPbI_3$. The banks were necessary to avoid the use of photolithography processes directly on the hybrid perovskite because the $MAPbI_3$ is vulnerable to wet processes.
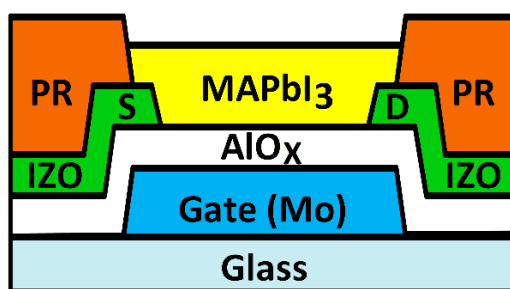

Figure 1. Schematic cross-section of the $MAPbI_3$ thin-film transistors (TFTs). During spin coating, the $MAPbI_3$ sink into holes ("banks") formed in the photoresist (PR) layer. The source (S) and drain (D) electrodes are made of indium zinc oxide (IZO) and the gate insulator is AlO_x.

After the formation of the banks, we subjected the samples to UV-ozone treatment (AHTECH LTS., Gyeonggi-do, South Korea) for 15 min before depositing the $MAPbI_3$ in ambient air (at 25 °C and relative humidity of ~52%). The UV-ozone treatment modifies the surface of the AlO_x G.I. for better $MAPbI_3$ adhesion. To make the $MAPbI_3$ solution, we dissolved precursors CH_3NH_3I (99.999%) (Greatcell Solar, Queanbeyan, Australia) and PbI_2 (99.999%, Sigma-Aldrich) (1:1 molar ratio) (manufacturer, city, Country) in N, N dimethylformamide anhydrous, DMF (99.8%) (Merck Korea Ltd./Sigma-Aldrich Korea Ltd.), and added 50 μL of hydriodic acid (57 wt%) (Merck Korea Ltd./Sigma-Aldrich Korea Ltd.). We used $MAI:PbI_2$ ratios of 0.5:1, 0.8:1, 1:1, and 1.2:1 and stirred the solutions for six hours at 60°C before spin-coating in ambient air. The spin-coating speed and time were respectively 6000 rpm and 70 s,

achieving a thickness of ~130 nm for the MAPbI$_3$. During the spin-coating process, we added 150 μL of toluene (99.8%, Sigma-Aldrich) (Merck Korea Ltd./Sigma-Aldrich Korea Ltd.) as an anti-solvent. The toluene reduces the crystallization time by rapidly reducing the solubility of the MAPbI$_3$, thereby promoting fast nucleation and growth of crystals in the film.

As the MAPbI$_3$ solutions sunk into the holes in the PR layer (Figure 1), it was not necessary to pattern the MAPbI$_3$ films through photolithography. Note that direct photolithography on these hybrid materials may lead to contamination. Finally, we annealed the samples at 115 °C for 10 min on a hotplate to finish the crystallization process. We analyzed the physical properties of the films using X-ray photoelectron spectroscopy (XPS) (ULVAC-PHI, INCORPORATED, PHI 5000 VersaProbe, Kanagawa, Japan), atomic force microscope (AFM) images (Park Systems, XE-100, Suwon, Korea), X-ray diffraction (XRD) (Malvern Panalytical Ltd, X'Pert PRO, Royston, UK) and scanning electron microscope (SEM) images (Hitachi High Technologies, S-4700, Tokyo, Japan). We respectively derived the μ$_{FE}$ and threshold voltage (V$_{TH}$) values from the slopes and intercepts of the linear regression lines of the I$_D$$^{1/2}$(V$_{GS}$) plots in the saturation region (V$_{DS}$ > V$_{GS}$ − V$_{TH}$), according to the equation, I$_D$ = (W/L)*C$_{OX}$*μ$_{FE}$*(V$_{GS}$ − V$_{TH}$)^2. Here, W, L, V$_{GS}$, V$_{DS}$, and I$_D$ denote the channel width, channel length, gate voltage, drain voltage, and drain current, respectively. We derived the μ$_{FE}$ and V$_{TH}$ from the |I$_{DS}$|$^{1/2}$(V$_{GS}$) plots. We estimated the subthreshold V$_{GS}$ swing (SS) by (d log (I$_D$)/d V$_{GS}$)$^{-1}$.

3. Results

Consistent with previous reports [34], the ambient air-processed MAPbI$_3$ films consisted of a network of thick dendritic bundles and the thickness of the bundles increased with increasing MAI/PbI$_2$ ratio (Figure 2). This dendritic structure is common to films exposed to humidity during processing and it indicates anisotropic growth, where faster growth occurs along energetically favorable crystallographic directions [34]. Despite the poor film coverage, dendritic bundles are known for their good film conductivity and are thus desirable for lateral conduction in solution processed semiconductors [34]. Each of the bundles exhibited good crystallinity as seen from the high resolution SEM images (Figure 2b,d,f,h) and XRD analysis.
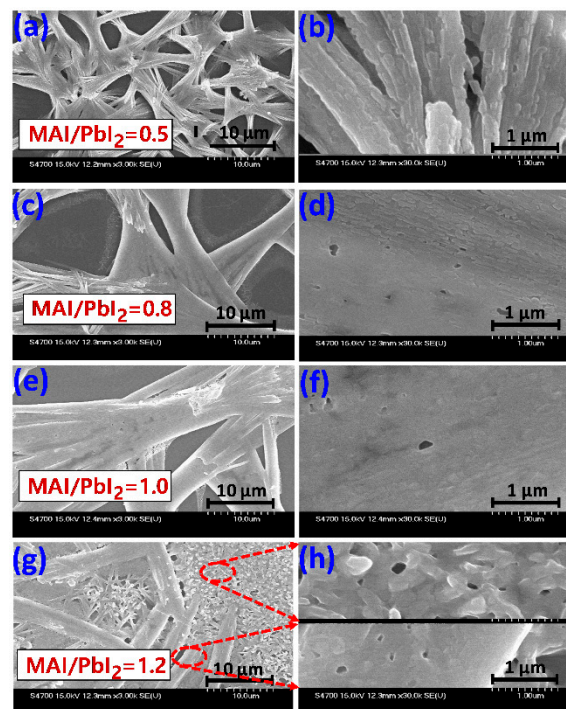

Figure 2. Scanning electron microscope (SEM) images of 10 μm and 1 μm magnification of MAPbI$_3$ films with varying MAI/PbI$_2$ ratios of (**a,b**) 0.5, (**c,d**) 0.8, (**e,f**) 1, and (**g,h**) 1.2.

XRD measurements verified that the films were MAPbI$_3$ films of the intended MAI/PbI$_2$ ratios. The XRD patterns of all the four ambient air-processed MAPbI$_3$ films contained sharp peaks at 2θ values of 13.9°, 28.2°, and 31.7°, the intensity of which increased with increasing MAI/PbI$_2$ ratio (Figure 3). These peaks are respectively assigned to the (110), (220) and the (310) crystal planes of the MAPbI$_3$ and they indicate high crystallinity in tetragonal phase [35]. Consistently, the intensity of the peak at the 2θ value of 12.67° gradually decreases with increasing MAI/PbI$_2$ ratio until it completely disappears when the ratio exceeds one. This is the PbI$_2$ peak and its absence indicates the absence of PbI$_2$ residues in the film [36–40].
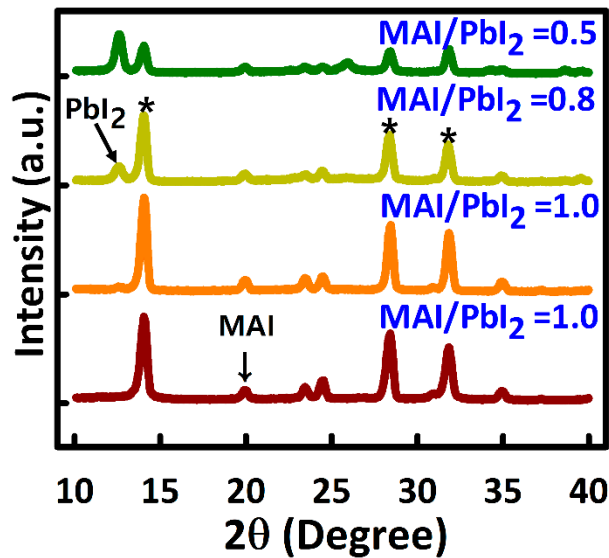

Figure 3. X-ray diffraction (XRD) patterns of MAPbI$_3$ films of varying MAI/PbI$_2$ ratio.

The AFM images of the AlO$_x$ and MAPbI$_3$ film (MAI/PbI$_2$ = 1.0) are shown in Figure 4a,b, respectively. The AlOx form a very smooth film with roughness of root mean square (rms) value approximately equal to 0.2 nm. However, the dendrites of the MAPbI$_3$ film results in a much higher rms value of the roughness, reaching 40 nm. The AlO$_x$ is amorphous (Figure 5a) and its atomic concentrations are shown in Figure 5b. Using a TFT structure (Figure 1), we measured the breakdown voltage of the AlOx gate insulator to be 4 MV/cm Figure 5c). These results are consistent with previous reports [41].
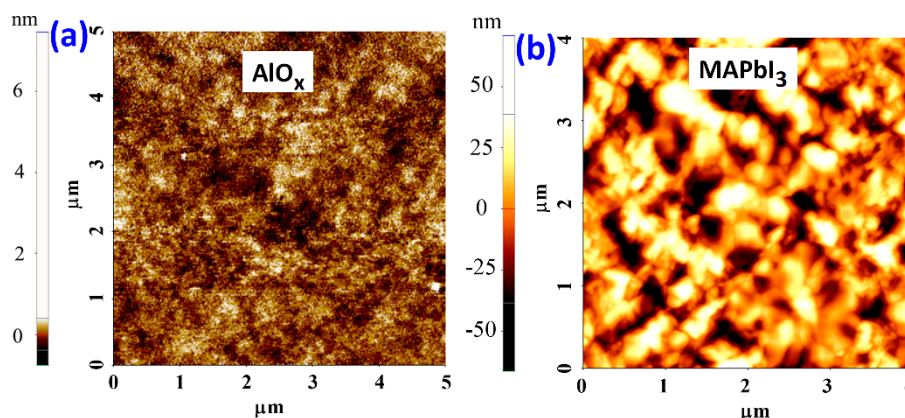

Figure 4. Atomic force microscope (AFM) images of the (**a**) AlO$_x$ and (**b**) MAPbI$_3$ layer (MAI/PbI$_2$ = 1.0) solution processed in ambient air.
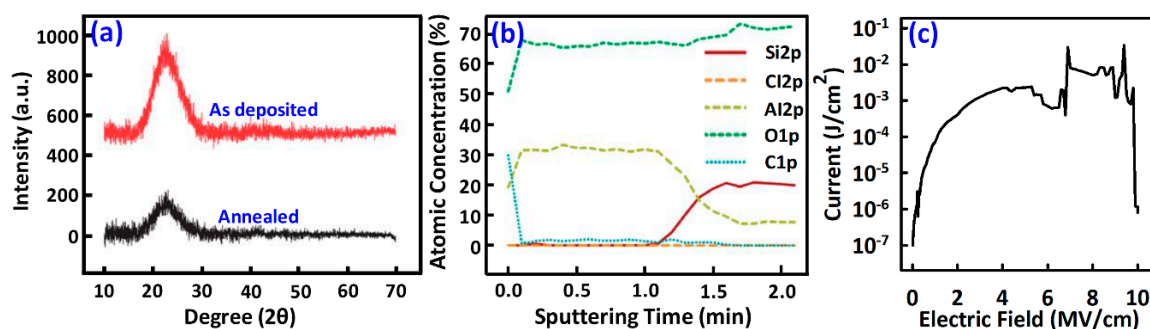
Figure 5. (**a**) XRD patterns of the solution processed AlO_x layer as deposited (**top**), and after 350 °C annealing (**bottom**). (**b**) XPS spectra of the solution processed AlO_x layer after annealing at 350 °C. Current–voltage (J–V) characteristics of the AlO_x layer showing a breakdown voltage of approximately 4 MV/cm.

We observed clear room temperature ambipolar transport in the $MAPbI_3$ TFTs. In unipolar enhancement mode TFTs, negligible I_D flows across the channel when the V_{GS} is equal to zero volts, unless the V_{GS} is increased to a value greater than the V_{TH}. For the $MAPbI_3$ TFTs investigated herein, however, the I_D increases rapidly with increasing $|V_{DS}|$ when $V_{GS} = 0$ V (Figure 6). Under p-type bias conditions [Figure 6a], for instance, electrons are injected from the drain to the source for $V_{DS} <$ (V_{GS}–V_{THn}). Here V_{THn} is the V_{TH} for the n-type characteristics. The flow of current at $V_{GS} = 0$ V is due to the presence of both hole and electron transport, and the choice of the carrier is determined by the equivalent bias conditions as shown in Figure 7.
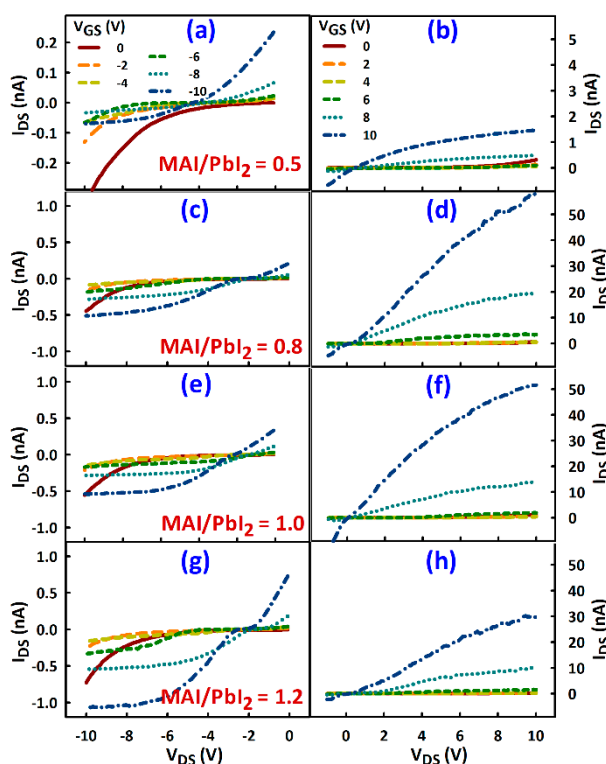

Figure 6. P-type and n-type output characteristics (I_D vs. V_{DS} plots) of a $MAPbI_3$ TFTs with MAI/PbI_2 ratio of (**a,b**) 0.5, (**c,d**) 0.8, (**e,f**) 1.0, and (**g,h**) 1.2. W = 100 μm and L = 50 μm.
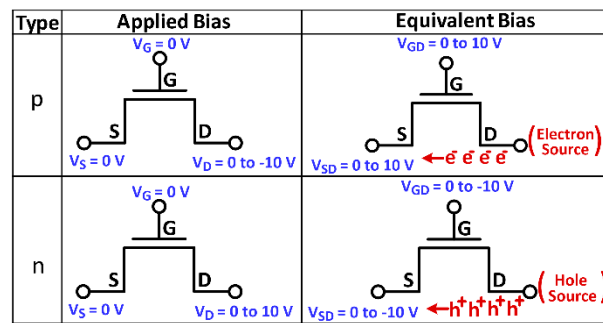
Figure 7. Effect of bias in the ambipolar MAPbI$_3$ TFTs.

When the V_{DS} is swept from 0 to −10 V with the V_{GS} fixed at zero volts, the equivalent bias conditions favor electron injection from the drain (see p-type characteristics in Figure 7). If the semiconductor supports bipolar transport, electron transport will dominate conduction under these bias conditions. This is the case for the MAPbI$_3$ studied herein. The electron current under the p-type bias conditions (when $V_{DS} < (V_{GS} - V_{THn})$) is similar to that of a TFT in the diode configuration (i.e., $V_{GS} = V_{DS}$. Although in saturation ($V_{DS} > V_{GS} - V_{TH}$), the I_D does not level-off but continues to exponentially increase with V_{DS} in a manner similar to the current of a forward biased diode). As the V_{GS} decreases from 0 to -6 V, the electron injection from the drain is shifted to smaller and smaller values of V_{DS} because negative V_{GS} depletes electrons. With further decrease in V_{GS} (−8 to −10 V), holes accumulate in the channel and the injection of holes from the source to the drain is initiated. Under the hole transport, the output curves saturate at $V_{DS} = (V_{GS} - V_{THp})$, where V_{THp} is the V_{TH} for the p-type characteristics (Figure 6a). Note that the direction of the current is the same for both the electron and hole transport (i.e., from the source to the drain). The significance of this is that the simultaneous or selective transport of electrons and/or holes is possible, depending on the bias conditions. Similarly, injection of holes from the drain is obtained under the n-type bias conditions when $V_{GS} = 0$ V and $V_{DS} > (V_{GS} - V_{THp})$. The hole current under the n-type bias conditions is also similar to that of a TFT in the diode configuration (Figure 6b). With increasing V_{GS}, hole injection from the drain shifts towards larger and larger values of V_{DS} until electrons are the dominant carriers, and the output curves saturate at $V_{DS} = (V_{GS} - V_{THn})$.

It is interesting to see here that the ambipolar transport is apparent in all MAI/PbI$_2$ ratios investigated (Figure 6a–h). However, the precursor composition has a clear effect on the magnitudes of each carrier transport. Hole and electron current increase with increasing MAI/PbI$_2$ ratio, which is an indication of increased structural order in the MAPbI$_3$ film with the increasing ratio. However, the electron transport appears to reach a peak when the MAI/PbI$_2$ ratio 0.8, and decreases thereafter.

4. Discussion

A distinct characteristic of the MAPbI$_3$ TFTs studied herein is the low driving voltages and stable room temperature operation. While the former is due to the thin high-k AlO$_x$ gate insulator, the latter is related to the ambient air processing. Ambient oxygen has been reported to have a passivation effect on the defects in perovskite materials [34,42,43]. It is also important to note that the ambipolar transport in the MAPbI$_3$ is unbalanced. For MAI/PbI$_2$ = 0.5, the electron current is about twenty times larger than the hole current (Figure 6a,b). Although the current of both carriers increases with increasing ratio, the electron current (I_e) increases much faster compared to the hole current (I_h), such that the I_e becomes about one hundred times larger than the I_h when the ratio reaches 0.8 (Figure 6e,f). However, the electron current appears to saturate, while the hole current continues to increase, when the ratio exceeds 0.8, such that the electron current becomes only fifty times larger than the hole current when the ratio reached 1.2.

We have recently shown that that small amounts of residual PbI_2 (as in the case of MAI/PbI_2 = 0.8) may boost electron transport and minimize ion migration by passivating ion vacancy defects in grain boundaries [44]. These ion vacancy defects are pathways for ion migration and their passivation improves lateral conduction and minimizes the vacancy-mediated migration of ions in the $MAPbI_3$ film. This could be the reason for the high I_e exhibited by the TFTs with MAI/PbI_2 = 0.8.

The ambipolar nature of the $MAPbI_3$ also shows in the TFT transfer characteristics (Figure 8). The transfer characteristics are semi-log plots of the $|I_D|$ as a function of the V_{GS} and they describe ON and OFF (switching) characteristics of the TFTs. In unipolar p-type TFTs, for example, negative V_{GS} pushes the fermi level (E_F) towards the valence band (E_V). The μ_{FE}, V_{TH} and SS values extracted from the saturation characteristics are shown in Figure 9. In the ON state, the I_D due to the flow of electrons is over an order of magnitude larger than that due to the flow of holes, for all ratios (Figure 8). Furthermore, the ON/OFF ratio of the p-type transfer characteristics is about two orders of magnitude, whereas that of the n-type transfer characteristics is about five orders of magnitude. Consistently; the electron μ_{FE} is two orders of magnitude larger than that of the holes (Figure 9a,b).
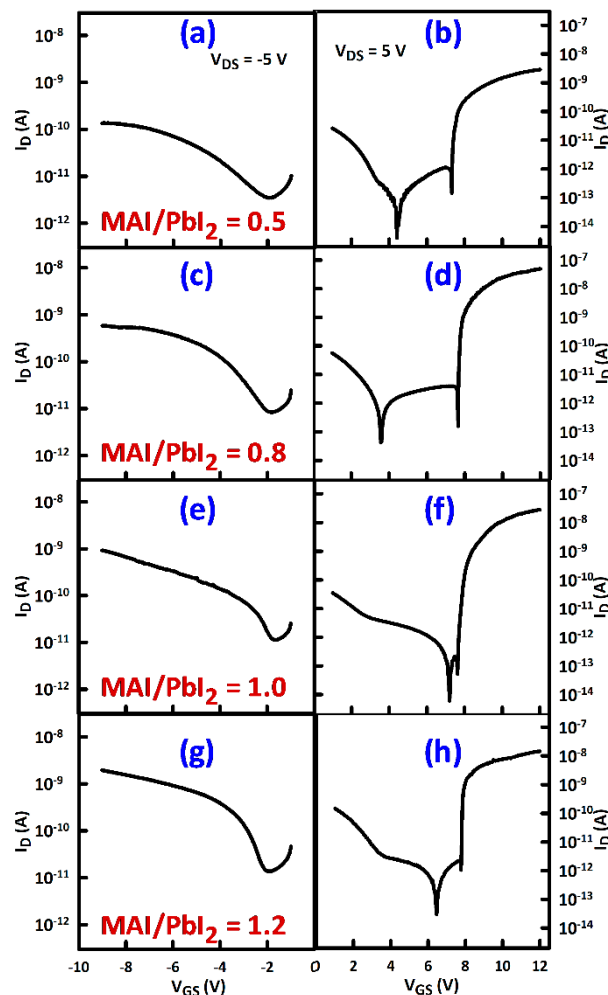

Figure 8. P-type and n-type transfer characteristics ($\log|I_D|$ vs. V_{GS} plots) of a $MAPbI_3$ TFTs with MAI/PbI_2 ratio of (**a,b**) 0.5, (**c,d**) 0.8, (**e,f**) 1.0, and (**g,h**) 1.2. W = 100 μm and L = 50 μm.

Under the n-type bias conditions, the I_D is due to holes flowing from the drain to the source, when the V_{GS} is close to zero volts. Increasing the V_{GS} positively results in the depletion of the holes and hence the decrease in I_D. However, this off-state current is a sum of channel, gate leakage (I_G) and displacement currents. As a result, negative current can be recorded at the drain when the I_G

dominates the three, which is the reason for the small hump in the n-type semi-log plots of $|I_D|$ (see Figure 8b,d,f,h). This hump comes from $|I_G|$ before the TFT turns ON. When the V_{GS} is greater than seven volts, the accumulation of electrons is initiated and the I_D is due to electrons flowing from the source to the drain. The concentration of these electrons increases with V_{GS} and the opposite is true for the hole current.
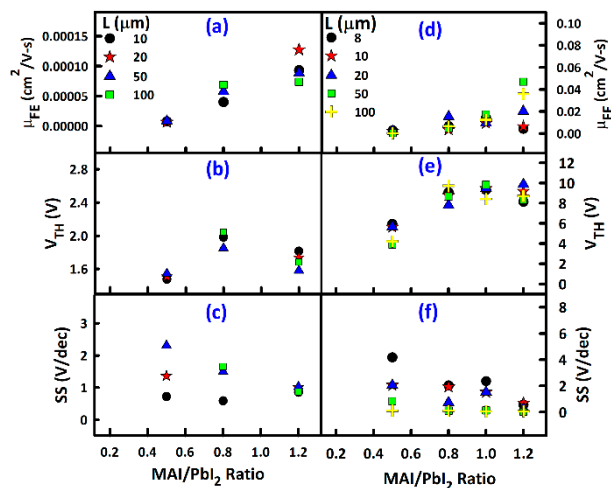

Figure 9. Extracted TFT parameters. (**a–c**) P-type and (**d–f**) n-type.

The I_G of the TFTs presented herein is quite significant, given the relatively low ON state currents of the TFTs. Figure 10 shows the transfer characteristics of TFTs with varying channel length (L) and the I_G curves for the MAI/PbI$_2$ ratio of 1.2. The MAI/PbI$_2$ ratio of 1.2 is shown here because it achieves the highest I_h. The I_D scaled proportionally with L for both the hole (Figure 10a) and electron (Figure 10b) transport. For both p-type and n-type characteristics, the I_G ranges from 0.1 to 1 nA in the ON state. The relatively high I_G is due to the thin (40 nm) gate insulator and can be decreased by increasing the thickness of the gate insulator.
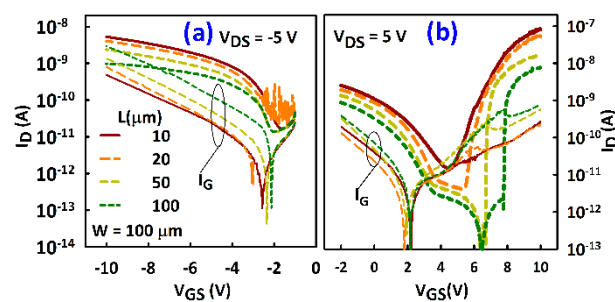

Figure 10. Transfer characteristics (log $|I_D|$ vs V_{GS}) and I_G curves for TFTs with a channel width (W) of 100 μm and varying channel length (L). (**a**) The p-type and (**b**) n-type bias conditions. MAI/PbI$_2$ = 1.2.

To separate the contact resistance (R_{CON}) from the channel resistance (R_{CH}), we used the "channel resistance" method [45]. In this method, it is assumed that the overall device resistance ($R_{TOT} = V_{DS}/I_D$) is given by the sum of the effective channel resistance, $R_{CH}*L_{EFF}$, and R_{CON}. R_{CH} is supposed to be gate modulated, while R_{CON} and L_{EFF} (the effective L) are assumed to be independent from the V_{GS}, such that the overall resistance is given by R_{TOT} (V_{GS}) = R_{CH} (V_{GS})*L_{EFF} + R_{CON}. For a given V_{GS}, using the linear least-squares method, it is possible to determine $R_{CH}(V_{GS})$ by fitting R_{TOT} against L_{MASK}, as shown in Figure 11a,b). The gradient gives the R_{CH} at each V_{GS} (Figure 11c,d).

The R_{CH} ranges from 5–11 and 44–55 MΩ/μm, respectively for the electron and hole transport (Figure 11c,d). The R_{CON} is approximated to be 59 and 245 MΩ, respectively for the electron and

hole transport. The large R_{CON}, low ON state current and low μ_{FE} exhibited by these TFTs could be related to the existence of an injection barrier (φ_B) at the S/D-to-MAPbI$_3$ contact (schottky contact) (Figure 12). A consequent of this is the current crowding that occurs in the output characteristics of the TFTs (Figure 6). Consistent with previous reports [30], the effect of the MAI/PbI$_2$ ratio on the electrical properties of the TFTs indicate a shifting of the Fermi level (E_F) towards the valence band (E_V) with increasing MAI/PbI$_2$ ratio (Figure 12). For MAI/PbI$_2$ = 0.5, for instance, the film is n-type but highly resistive because of the excess PbI$_2$. Furthermore, the IZO-MAPbI$_3$ contact is schottky, given that Ψ_M is much larger than Ψ_S. On the other hand, the film processed with MAI/PbI$_2$ = 1.2 is almost p-type but the contact in also schottky, given that Ψ_M should be much larger than Ψ_S to achieve an ohmic contact for hole transport (Figure 12).
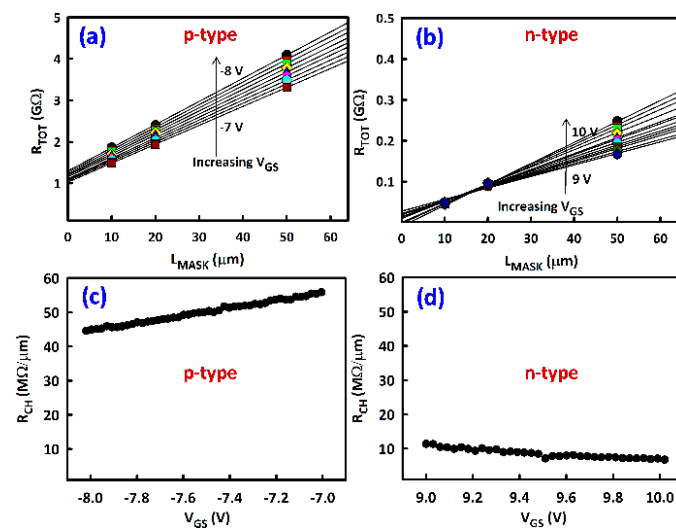

Figure 11. Extraction of channel resistance (R_{CH}). (**a**,**b**) Linear regression of the TFT's total resistance ($R_{TOT} = V_{DS}/I_D$), as a function of the design channel length (L_{MASK}) for (**a**) p-type, and (**b**) n-type characteristics. (**c**,**d**) R_{CH} per micrometer (of L) as a function of L_{MASK} for (**c**) p-type and (**d**) n-type characteristics.

　　The larger R_{CON} for hole, as opposed to electron transport, corresponds to a larger voltage drop at the S/D-to-MAPbI$_3$ contact, which may be the reason for the lower ON state current and the smaller μ_{FE} values. The large R_{CON} is the reason for the strong dependency of the μ_{FE} on L for the hole transport (Figure 9a). A possible origin for the large variation in the other TFT parameters (Figure 9) could be ion migration in the MAPbI$_3$ film [44]. As ion migration causes hysteresis in the current-voltage characteristics, the extracted TFT parameters may vary depending on the bias history of the devices. In addition, the devices presented herein do not have a passivation layer to protect the MAPbI$_3$ film from environmental contamination. The variation in extracted parameters could thus be due to environmental changes. However, it is interesting to see that the TFTs are stable and work very well in ambient air, despite the absence of a passivation layer.

　　It is also important to note that the achievement of an ohmic contact for one carrier type consequently achieves a schottky contact for the other, given that ohmic contacts are achieved with a high metal workfunction for the hole transport and a low metal workfunction for the electron transport. Another important factor to consider for the ambipolar transport of the TFTs is the initial position of the E_F, which may be determined by the MAI/PbI$_2$ ratio and fabrication process conditions (Figure 12). Variation in carrier concentration by varying the precursor ratio have also been previously reported [30]. Therefore, balanced carrier transport may be achieved by varying the precursor ratio and by proper source/drain electrode selection for each carrier type.
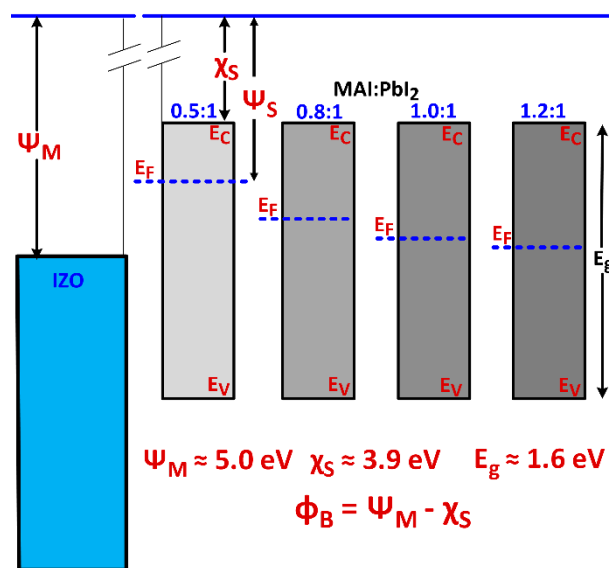
Figure 12. Band diagrams for the IZO and MAPbI$_3$ films of varying MAI/PbI$_2$ ratio. ψ_m, ψ_s, χ_s, and E$_g$ are the metal (IZO) workfunction, semiconductor (MAPbI$_3$) workfunction, electron affinity of the MAPbI$_3$, and band gap of the MAPbI$_3$, respectively.

5. Conclusions

The MAPbI$_3$ TFTs investigated herein exhibited ambipolar transport, where simultaneous or selective transport of electrons and/or holes was possible in a single device, depending on the applied bias. However, the electron transport (n-type) was slightly more pronounced than the hole transport (p-type), and the on-state current of the n-type and p-type TFTs was highest in the slightly PbI$_2$-rich and MAI-rich films, respectively, suggesting controllable n-type or p-type transport by precursor ratio. Furthermore, the use of different types of source/drain electrodes for each carrier type is necessary to balance the ambipolar transport.

6. Patents

CMOS DEVICE USING AMBIPOLAR ORGANIC-INORGANIC HYBRID PEROVSKITE AND METHOD OF MANUFACTURING THE SAME.

References

1. Chen, Q.; De Marco, N.; Yang, Y.M.; Song, T.B.; Chen, C.C.; Zhao, H.; Yang, Y. Under the spotlight: The organic–inorganic hybrid halide perovskite for optoelectronic applications. *Nano Today* **2015**, *10*, 355–396. [CrossRef]
2. Chin, X.Y.; Cortecchia, D.; Yin, J.; Bruno, A.; Soci, C. Lead iodide perovskite light-emitting field-effect transistor. *Nat. Commun.* **2015**, *6*, 7383. [CrossRef] [PubMed]

3. Lee, M.M.; Teuscher, J.; Miyasaka, T.; Murakami, T.N.; Snaith, H.J. Efficient hybrid solar cells based on meso-superstructured organometal halide perovskites. *Science* **2012**, *338*, 643–647. [CrossRef] [PubMed]

4. Ling, H.; Liu, S.; Zheng, Z.; Yan, F. Organic Flexible Electronics. *Small Methods* **2018**, *2*, 1800070. [CrossRef]

5. Polman, A.; Knight, M.; Garnett, E.C.; Ehrler, B.; Sinke, W.C. Photovoltaic materials: Present efficiencies and future challenges. *Science* **2016**, *352*, aad4424. [CrossRef] [PubMed]

6. He, Y.; Galli, G. Perovskites for solar thermoelectric applications: A first principle study of CH3NH3AI3 (A = Pb and Sn). *Chem. Mater.* **2014**, *26*, 5394–5400. [CrossRef]

7. Chen, W.; Wu, Y.; Yue, Y.; Liu, J.; Zhang, W.; Yang, X.; Chen, H.; Bi, E.; Ashraful, I.; Grätzel, M.; et al. Efficient and stable large-area perovskite solar cells with inorganic charge extraction layers. *Science* **2015**, *350*, 944–948. [CrossRef]

8. Cho, H.; Jeong, S.-H.; Park, M.-H.; Kim, Y.-H.; Wolf, C.; Lee, C.-L.; Heo, J.H.; Sadhanala, A.; Myoung, N.; Yoo, S.; et al. Overcoming the electroluminescence efficiency limitations of perovskite light-emitting diodes. *Science* **2015**, *350*, 1222–1225. [CrossRef]

9. Deschler, F.; Price, M.; Pathak, S.; Klintberg, L.E.; Jarausch, D.-D.; Higler, R.; Hüttner, S.; Leijtens, T.; Stranks, S.D.; Snaith, H.J.; et al. High photoluminescence efficiency and optically pumped lasing in solution-processed mixed halide perovskite semiconductors. *J. Phys. Chem. Lett.* **2014**, *5*, 1421–1426. [CrossRef]

10. Zhu, H.; Fu, Y.; Meng, F.; Wu, X.; Gong, Z.; Ding, Q.; Gustafsson, M.V.; Trinh, M.T.; Jin, S.; Zhu, X.-Y. Lead halide perovskite nanowire lasers with low lasing thresholds and high quality factors. *Nat. Mater.* **2015**, *14*, 636–642. [CrossRef]

11. Stranks, S.D.; Snaith, H.J. Metal-halide perovskites for photovoltaic and light-emitting devices. *Nat. Nanotechnol.* **2015**, *10*, 391–402. [CrossRef] [PubMed]

12. Sadhanala, A.; Deschler, F.; Thomas, T.H.; Dutton, S.E.; Goedel, K.C.; Hanusch, F.C.; Lai, M.L.; Steiner, U.; Bein, T.; Docampo, P.; et al. Preparation of single-phase films of CH3NH3Pb (I1–xBrx) 3 with sharp optical band edges. *J. Phys. Chem. Lett.* **2014**, *5*, 2501–2505. [CrossRef] [PubMed]

13. Shi, D.; Adinolfi, V.; Comin, R.; Yuan, M.; Alarousu, E.; Buin, A.; Chen, Y.; Hoogland, S.; Rothenberger, A.; Katsiev, K.; et al. Low trap-state density and long carrier diffusion in organolead trihalide perovskite single crystals. *Science* **2015**, *347*, 519–522. [CrossRef] [PubMed]

14. Sadhanala, A.; Ahmad, S.; Zhao, B.; Giesbrecht, N.; Pearce, P.M.; Deschler, F.; Hoye, R.L.Z.; Gödel, K.C.; Bein, T.; Docampo, P.; et al. Blue-green color tunable solution processable organolead chloride–bromide mixed halide perovskites for optoelectronic applications. *Nano Lett.* **2015**, *15*, 6095–6101. [CrossRef] [PubMed]

15. Tan, Z.-K.; Moghaddam, R.S.; Lai, M.L.; Docampo, P.; Higler, R.; Deschler, F.; Price, M.; Sadhanala, A.; Pazos, L.M.; Credgington, D.; et al. Bright light-emitting diodes based on organometal halide perovskite. *Nat. Nanotechnol.* **2014**, *9*, 687–692. [CrossRef]

16. Klauk, H. Organic thin-film transistors. *Chem. Soc. Rev.* **2010**, *39*, 2643–2666. [CrossRef]

17. Wu, Y.; Li, J.; Xu, J.; Du, Y.; Huang, L.; Ni, J.; Cai, H.; Zhang, J. Organic–inorganic hybrid CH3NH3PbI3 perovskite materials as channels in thin-film field-effect transistors. *RSC Adv.* **2016**, *6*, 16243–16249. [CrossRef]

18. Ngai, J.H.L.; Ho, J.K.W.; Chan, R.K.H.; Cheung, S.H.; Leung, L.M.; So, S.K. Growth, characterization, and thin film transistor application of CH3NH3PbI3 perovskite on polymeric gate dielectric layers. *RSC Adv.* **2017**, *7*, 49353–49360. [CrossRef]

19. Xu, J.; Li, J.; Tang, L.; Peng, Y.; Wu, Y.; Du, Y.; Huang, L.; Ni, J.; Cai, H.; Zhang, J. The optimization of organic–inorganic perovskite films by annealing atmosphere for applications in transistors. *Phys. Status Solidi* **2017**, *214*, 1700170. [CrossRef]

20. Peng, Y.; Tang, L.; Zhou, Z.; Xu, J.; Li, J.; Cai, H.; Ni, J.; Zhang, J. Enhancing perovskite TFTs performance by optimizing the interface characteristics of metal/semiconductor contact. *J. Phys. D Appl. Phys.* **2018**, *51*, 445101. [CrossRef]

21. Tang, L.; Peng, Y.; Zhou, Z.; Wu, Y.; Xu, J.; Li, J.; Du, Y.; Huang, L.; Cai, H.; Ni, J.; et al. High-performance organic–inorganic hybrid perovskite thin-film field-effect transistors. *Appl. Phys. A* **2018**, *124*, 624. [CrossRef]

22. Baikie, T.; Fang, Y.; Kadro, J.M.; Schreyer, M.; Wei, F.; Mhaisalkar, S.G.; Grätzel, M.; White, T.J. Synthesis and crystal chemistry of the hybrid perovskite (CH$_3$NH$_3$) PbI$_3$ for solid-state sensitised solar cell applications. *J. Mater. Chem. A* **2013**, *1*, 5628–5641. [CrossRef]

23. Yamada, Y.; Nakamura, T.; Endo, M.; Wakamiya, A.; Kanemitsu, Y. Near-band-edge optical responses of solution-processed organic–inorganic hybrid perovskite CH$_3$NH$_3$PbI$_3$ on mesoporous TiO$_2$ electrodes. *Appl. Phys. Express* **2014**, *7*, 032302. [CrossRef]

24. Fang, H.-H.; Raissa, R.; Abdu-Aguye, M.; Adjokats, S.; Blake, G.R.; Even, J.; Loi, M.A. Photophysics of Organic–Inorganic Hybrid Lead Iodide Perovskite Single Crystals. *Adv. Funct. Mater.* **2015**, *25*, 2378. [CrossRef]

25. Oga, H.; Saeki, A.; Ogomi, Y.; Hayase, S.; Seki, S. Improved Understanding of the Electronic and Energetic Landscapes of Perovskite Solar Cells: High Local Charge Carrier Mobility, Reduced Recombination, and Extremely Shallow Traps. *J. Am. Chem. Soc.* **2014**, *136*, 13818–13825. [CrossRef]

26. Savenije, T.J.; Ponseca, C.S.; Kunneman, L.; Abdellah, M.; Zheng, K.; Tia, Y.; Zhu, Q.; Canton, S.E.; Scheblykin, I.G.; Pullerits, T.; et al. Thermally Activated Exciton Dissociation and Recombination Control the Carrier Dynamics in Organometal Halide Perovskite. *J. Phys. Chem. Lett.* **2014**, *5*, 2189–2194. [CrossRef]

27. Wehrenfennig, C.; Liu, M.; Snaith, H.J.; Johnston, M.B.; Herz, L.M. Charge-carrier dynamics in vapour-deposited films of the organolead halide perovskite CH$_3$NH$_3$PbI$_{3-x}$Cl$_x$. *Energy Environ. Sci.* **2014**, *7*, 2269–2275. [CrossRef]

28. Noh, J.H.; Im, S.H.; Heo, J.H.; Mandal, T.N.; Seok, S.I. Chemical management for colorful, efficient, and stable inorganic–organic hybrid nanostructured solar cells. *Nano Lett.* **2013**, *13*, 1764–1769. [CrossRef]

29. Capelli, R.; Toffanin, S.; Generali, G.; Usta, H.; Facchetti, A.; Muccini, M. Organic light-emitting transistors with an efficiency that outperforms the equivalent light-emitting diodes. *Nat. Mater.* **2010**, *9*, 496–503. [CrossRef]

30. Wang, Q.; Shao, Y.; Xie, H.; Lyu, L.; Liu, X.; Gao, Y.; Huang, J. Qualifying composition dependent p and n self-doping in CH$_3$NH$_3$PbI$_3$. *Appl. Phys. Lett.* **2014**, *105*, 163508. [CrossRef]

31. Senanayak, S.P.; Yang, B.; Thomas, T.H.; Giesbrecht, N.; Huang, W.; Gann, E.; Nair, B.; Goedel1, K.; Guha, S.; Moya, X.; et al. Understanding charge transport in lead iodide perovskite thin-film field-effect transistors. *Sci. Adv.* **2017**, *3*, e1601935. [CrossRef] [PubMed]

32. Hoang, N.T.T.; Haque, F.; Ji, J.; Mativenga, M. Fast-Switching Mixed A-Cation Organic-Inorganic Hybrid Perovskite TFTs. *IEEE Electron Device Lett.* **2019**, *40*, 917–920. [CrossRef]

33. Yusoff, A.R.B.M.; Kim, H.P.; Li, X.; Kim, J.; Jang, J.; Nazeeruddin, M.K. Ambipolar Triple Cation Perovskite Field Effect Transistors and Inverters. *Adv. Mater.* **2016**, *29*, 1602940. [CrossRef]

34. Cheng, Y.; So, F.; Tsang, S.-W. Progress in air-processed perovskite solar cells: From crystallization to photovoltaic performance. *Mater. Horiz.* **2019**, *6*, 1611–1624. [CrossRef]

35. Chen, Q.; Zhou, H.; Hong, Z.; Luo, S.; Duan, H.-S.; Wang, H.-H.; Liu, Y.; Li, G.; Yang, Y. Planar Heterojunction Perovskite Solar Cells via Vapor-Assisted Solution Process. *J. Am. Chem. Soc.* **2014**, *136*, 622–625. [CrossRef]

36. Xiao, M.; Huang, F.; Huang, W.; Dkhissi, Y.; Zhu, Y.; Etheridge, J.; Gray-Weale, A.; Bach, U.; Cheng, Y.-B.; Spiccia, L. A Fast Deposition-Crystallization Procedure for Highly Efficient Lead Iodide Perovskite Thin-Film Solar Cells. *Angew. Chem. Int. Ed.* **2014**, *53*, 9898–9903. [CrossRef]

37. Burschka, J.; Pellet, N.; Moon, S.-J.; Humphry-Baker, R.; Gao, P.; Nazeeruddin, M.K.; Gratzel, M. Sequential deposition as a route to high-performance perovskite-sensitized solar cells. *Nature* **2013**, *499*, 316–319. [CrossRef]

38. Long, M.; Zhang, T.; Chai, Y.; Ng, C.-F.; Mak, T.C.W.; Xu, J.; Yan, K. Nanstoichiometric acid-base reaction as reliable synthetic route to highly stable CH$_3$NH$_3$PbI$_3$ perovskite film. *Nat. Com.* **2016**, *7*, 13503. [CrossRef]

39. Luo, S.; Daoud, W.A. Crystal Structure Formation of CH$_3$NH$_3$PbI$_{3-x}$Cl$_x$ Perovskite. *Materials* **2016**, *9*, 123. [CrossRef]

40. Ball, J.M.; Lee, M.M.; Hey, A.; Snaith, H.J. Low-temperature processed meso-superstructured to thin-film perovskite solar cells. *Energy Environ. Sci.* **2013**, *6*, 1739–1743. [CrossRef]

41. Wang, B.; Huang, W.; Chi, L.; Al-Hashimi, M.; Marks, T.J.; Facchetti, A. High-k Gate Dielectrics for Emerging Flexible and Stretchable Electronics. *Chem. Rev.* **2018**, *118*, 5690–5754. [CrossRef] [PubMed]

42. Meggiolaro, D.; Mosconi, E.; Angelis, F.D. Mechanism of Reversible Trap Passivation by Molecular Oxygen in Lead-Halide Perovskites. *ACS Energy Lett.* **2017**, *2*, 2794–2798. [CrossRef]

43. Lu, D.; Zhang, Y.; Lai, M.; Lee, A.; Xie, C.; Lin, J.; Lei, T.; Lin, Z.; Kley, C.S.; Huang, J.; et al. Giant Light-Emission Enhancement in Lead Halide Perovskite by Surface Oxygen Passivation. *Nano Lett.* **2018**, *18*, 6967–6973. [CrossRef] [PubMed]

44. Haque, F.; Hoang, N.T.T.; Ji, J.; Mativenga, M. Effect of Precursor Composition on Ion Migration in Hybrid Perovskite TFTs. *IEEE Electron Device Lett.* **2019**. [CrossRef]

45. Bhattacharya, P.; Bari, M.; Rao, K. Comparison of measurement techniques for gate shortening in sub-micrometer metal oxide semiconductor field effect transistors. *Jpn. J. Appl. Phys.* **1993**, *32*, 3409–3413. [CrossRef]